Pergamon

0301-9322(95)00042-9

Int. J. Multiphase Flow Vol. 21, No. 6, pp. 1203–1228, 1995

0301-9322/95 $9.50 + 0.00

GAS–PARTICLE TWO-PHASE TURBULENT FLOW IN A VERTICAL DUCT

J. CAO and G. AHMADI

Department of Mechanical and Aeronautical Engineering, Clarkson University, Potsdam, NY 13699-5725, U.S.A.

(Received 27 July 1994; in revised form 8 May 1995)

Abstract—Two-phase gas-phase turbulent flows at various loadings between the two vertical parallel plates are analyzed. A thermodynamically consistent turbulent two-phase flow model that accounts for the phase fluctuation energy transport and interaction is used. The governing equation of the gas-phase is upgraded to a two-equation low Reynolds number turbulence closure model that can be integrated directly to the wall. A no-slip boundary condition for the gas-phase and slip-boundary condition for the particulate phase are used. The computational model is first applied to dilute gas–particle turbulent flow between two parallel vertical walls. The predicted mean velocity and turbulence intensity profiles are compared with the experimental data of Tsuji *et al.* (1984) for vertical pipe flows, and good agreement is observed. Examples of additional flow properties such as the phasic fluctuation energy, phasic fluctuation energy production and dissipation, as well as interaction momentum and energy supply terms are also presented and discussed.

Applications to the relatively dense gas–particle turbulent flows in a vertical channel are also studied. The model predictions are compared with the experimental data of Miller & Gidaspow and reasonable agreement is observed. It is shown that flow behavior is strongly affected by the phasic fluctuation energy, and the momentum and energy transfer between the particulate and the fluid constituents.

Key Words: two-phase flow, gas–particle flow, turbulent flow, duct flow

INTRODUCTION

Multiphase systems, in general, and two-phase turbulent flows, in particular, are of considerable engineering importance, and have a wide range of industrial applications. Typical examples related to the coal energy system are pre-combustion mixing of pulverized coal and particle laden flows in coal gasifiers. In addition, two-phase flows occur in pneumatic transport of powder, spray combustion systems and in flows during loss-of-coolant accidents in pressurized-water nuclear reactors, as well as sediment transports in rivers and aeolian transport in dessert and many other fields.

Modeling two-phase flow has attracted considerable interest in the past three decades. Extensive reviews of earlier works were provided by Soo (1967), Wallis (1969) and Hetsroni (1982). Progress in continuum theories of two-phase flows were reported by Truesdell & Toupin (1960), Bowen (1967), Eringen & Ingram (1967), Nunziato & Walsh (1980), Ahmadi (1982, 1985), Massoudi (1986) and Johnson *et al.* (1991a, b) among others. Computational modeling of two-phase flows were studied by Gidaspow (1986), Gidaspow *et al.* (1989), Maeda *et al.* (1990) and Dasgupta *et al.* (1994) to name a few. For the past two decades, considerable advances have been made in understanding the dynamic behavior of turbulent multiphase flows. A number of models for dispersed two-phase turbulent flows were developed by Hetsroni & Sokolov (1972), Genchev & Karpuzov (1980), Elghobashi & Abou-Arab (1983), Chen & Wood (1985) and Kashiwa (1987), and certain numerical simulations were presented. However, these available models are generally limited to the case of dilute suspensions, where the role of inter-particle collision is negligible, and the effects of fluctuation kinetic energy of the particulate phase are also neglected. While Kashiwa (1987) and Sommerfeld *et al.* (1992) proposed more elaborate models that offered certain improvements, their models were not concerned with dense mixtures and particle collisional effects. Only recently, Tsuji *et al.* (1989a, b) and Louge *et al.* (1991) included the effect of inter-particle collisions, while using an idealized model for the fluid phase.

Experimental studies for dilute two-phase turbulent flow were reported by Hetsroni & Sokolov (1971), Popper & Abuaf (1974), Zisselmar & Molerus (1979), Modarress *et al.* (1982, 1983), Lee

& Durst (1982), Theofanous & Sullivan (1982) and Tsuji *et al.* (1982, 1984). However, experimental investigations of dense two-phase, solid–liquid mixtures are relatively scarce. In his pioneering work, Bagnold (1954) measured the particulate phasic stresses in a mixture of neutrally buoyant wax beads in water. Savage & McKeown (1983) and Hanes & Inman (1985) carried out a series of experiments on dense solid–liquid mixtures using a simple shear flow apparatus. Variations of shear and normal stresses with solid volume fraction and shear rates were measured. More recently, Gidaspow *et al.* (1991) and Miller & Gidaspow (1992) measured the particle mean velocity, mass flux and concentration for realtively dense gas–solid flow in a vertical pipe. In these studies, it was shown that there were significant differences between dilute and dense two-phase turbulent flows. The main differences are the mechanism of exchange of momentum and fluctuation kinetic energy between the particulate and the fluid phases. Due to the importance of inter-particle collisional effects, the dynamic behavior of dense two-phase turbulent flow is far more complicated than the dilute case.

Recently, Ahmadi & Ma (1990) used a phasic mass-weighted averaging technique to establish a thermomechanical formulation for turbulent multiphase flows. A closed system of field equations was obtained for determining the velocity, solid volume fraction and fluctuation kinetic energies of different phases. In particular, the formation includes distinct transport equations for the fluctuation kinetic energies of the particulate and fluid phases. This model also included the particulate collisional stresses and, therefore, is suitable for analyzing turbulent flows of relatively dense mixtures.

In the present work, the model of Ahmadi & Ma (1990) is used to analyze the steady, fully-developed, dilute and dense, two-phase gas–particle turbulent flow between two vertical parallel plates. The model for the gas-phase is upgraded to a two-equation low Reynolds number turbulence model. The no-slip boundary condition for gas-phase and the boundary conditions developed by Jenkins (1990), which allow for the slip of the particulate phase at the wall, are adopted in the present analysis. The resulting governing equations are solved by using a semi-implicit finite difference method. The computational model is first used to simulate dilute and relatively dense gas–particle turbulent flows in a vertical channel. In the absence of experimental data for flows between two vertical parallel plates, the model predictions for the phasic mean velocity, turbulence intensity, solid volume fraction and mass flux are compared with the experimental data of Tsuji *et al.* (1984) and Miller & Gidaspow (1992) for pipe flows. It is shown that the model predictions are in reasonable agreement with the experimental data. A simulation for gravity-driven gas–particle flows at high loading is also carried out. While there are no data available for comparison, the predicted results appear to be reasonable. The effects of gas loading, particle size and particle–wall friction coefficient are also studied.

GOVERNING EQUATIONS

The governing equations of two-phase turbulent flows as developed by Ahmadi & Ma (1990) and Ma & Ahmadi (1990) are used in this study. For a fully developed two-phase flow between two vertical parallel plates, the flow variables are only functions of y and t. A schematic of the flow region is shown in figure 1. It is assumed that the fluid and particulate constituents are incompressible and the flow is isothermal. In this case, the continuity equations for particulate and fluid phase are automatically satisfied. The momentum and fluctuation kinetic equations are then reduced to:

Momentum balance

Particulate phase

$$\rho_0 \nu \frac{\partial u}{\partial t} = -\rho_0 \nu g - \nu \frac{\mathrm{d}p^f}{\mathrm{d}x} + \frac{\partial}{\partial y}\left[(\mu + \mu^{\mathrm{T}})\frac{\partial u}{\partial y}\right] + D_0(u^f - u) \qquad [1]$$

$$-\nu \frac{\mathrm{d}p^{\mathrm{f}}}{\mathrm{d}y} - \frac{\partial(\gamma \rho_0 \nu k)}{\partial y} = 0 \qquad [2]$$

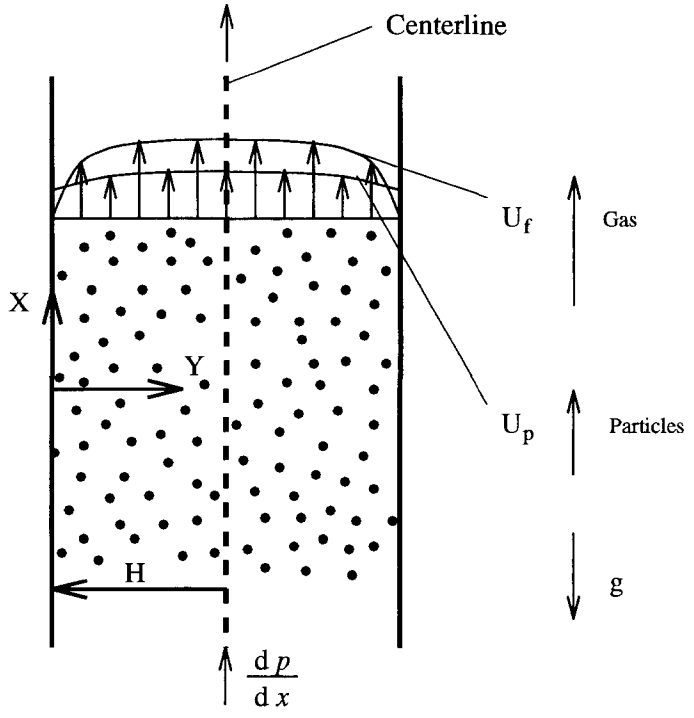

Figure 1. Flow field schematic.

Fluid phase

$$\rho_0^f v^f \frac{\partial u^f}{\partial t} = -\rho_0^f v^f g - v^f \frac{dp^f}{dx} + \frac{\partial}{\partial y}\left[(\mu^f + \mu^{fT})\frac{\partial u^f}{\partial y}\right] + D_0(u - u^f) \quad [3]$$

$$-v^f \frac{dp^f}{dy} - \frac{2}{3}\frac{\partial(\rho_0^f v^f k^f)}{\partial y} = 0 \quad [4]$$

Fluctuation kinetic energy balance

Particulate phase

$$\rho_0 \frac{\partial k}{\partial t} = \mu^T\left(\frac{\partial u}{\partial y}\right)^2 + \frac{\partial}{\partial y}\left(\frac{\mu^T}{\sigma^k}\frac{\partial k}{\partial y}\right) - \rho_0 v\epsilon + 2D_0(ck^f - k) \quad [5]$$

Fluid phase

$$\rho_0^f v^f \frac{\partial u^f}{\partial t} = \mu^{fT}\left(\frac{\partial u^f}{\partial y}\right)^2 + \frac{\partial}{\partial y}\left[\left(\mu^f + \frac{\mu^{fT}}{\sigma^{fk}}\right)\frac{\partial k^f}{\partial y}\right] - \rho_0^f v^f \epsilon^f + 2D_0(k - k^f) \quad [6]$$

Global continuity equation

$$v^f + v = 1. \quad [7]$$

In these equations, u is the mass-weighted average velocity, k is the fluctuation kinetic energy per unit mass, ϵ is the dissipation rate per unit mass, p^f is the mean pressure in the fluid phase, v is the solid volume fraction, ρ_0 is the constitutuent density, μ is the coefficient of viscosity, μ^T is the coefficient of turbulence (eddy) viscosity, g is the acceleration of gravity and σ^k is the turbulence Prandtl number for fluctuation kinetic energy. The superscript f refers to the fluid phase and a symbol without a superscript represents a particulate phase quantity.

The coefficients of turbulence viscosity and the dissipation rate for particulate phase are given as:

$$\mu^T = C^{*\mu} C^\mu \rho v \, dk^{1/2}, \quad \epsilon = ak^{3/2}, \quad [8]$$

where

$$C^{\mu} = 0.0853[(\chi\nu)^{-1} + 3.2 + 12.1824\nu\chi],$$

$$C^{*\mu} = \frac{1}{1 + \frac{T_L}{\tau}\left(1 - \frac{\nu}{\nu_m}\right)^3},$$

$$a = \frac{3.9\nu\chi(1 - r^2)}{d}. \qquad [9]$$

Here, it is assumed that the particles are spherical and nearly elastic with a diameter d and a coefficient of restitution r. The parameters T_L and τ are the Lagrangian time macro-scale and the particle relaxation time, and are given as:

$$T_L = \frac{0.165k^f}{\epsilon^f}, \quad \tau = \frac{\rho_0 \nu}{D_0}. \qquad [10]$$

The drag coefficient D_0 is given as:

$$D_0 = \frac{18\mu_0^f \nu}{d^2} \frac{[1 + 0.1(\mathrm{Re_d})^{0.75}]}{\left(1 - \frac{\nu}{\nu_m}\right)^{2.5\nu_m}}, \qquad [11]$$

in which the particle Reynolds number is defined as:

$$\mathrm{Re_d} = \frac{\rho^f d|u^f - u|}{\mu_0^f}. \qquad [12]$$

The coefficient $C^{*\mu}$ is introduced in [8] to account for the reduction of collisional effect as particle relaxation time becomes small.

The crowding effect of particles exhibits itself through the radial distribution function χ. For spherical particles, it was found that (Ma & Ahmadi 1986)

$$\chi = \frac{1 + 2.5\nu + 4.5904(\nu)^2 + 4.515439(\nu)^3}{\left[1 - \left(\frac{\nu}{\nu_m}\right)^3\right]^{0.678021}}, \qquad [13]$$

with $\mu_m = 0.64356$. The increase in the particulate pressure is accounted for through the parameter γ which is given as:

$$\gamma = \tfrac{2}{3}(1 + 4\nu\chi) + \tfrac{1}{3}(1 - r^2). \qquad [14]$$

In [5], the coefficient c is related to the ratio of the particle relaxation time to the Lagrangian time macro-scale of turbulence, i.e.

$$c = \frac{1}{1 + \frac{\tau}{T_L}}. \qquad [15]$$

For the phasic coefficient of mean viscosity, the following expressions as suggested by Abu-Zaid & Ahmadi (1993) are used:

$$\mu = \frac{\nu\mu_0^f}{\left(1 - \frac{\nu}{\nu_m}\right)^{2.5\nu_m}}, \quad \mu^f = \frac{\nu^f\mu_0^f}{\left(1 - \frac{\nu}{\nu_m}\right)^{2.5\nu_m}}. \qquad [16]$$

These coefficients of mean viscosity resemble those suggested by Ishii & Mishima (1984) and Sinclair & Jackson (1989), and are consistent with Einstein's equation for effective viscosity of dilute suspensions.

It should be emphasized that [5] and [6] account for the evolution and transport of phasic fluctuation energies, and their interactions. In particular, the interaction fluctuation energy supply model used allows the transfer of fluctuation energy between the phases. Thus, a dilute suspension of small particles in a turbulent will attain fluctuation energy even in the absence of particle collisions. Similarly, rapidly fluctuating particulate phase will drag the fluid and generate fluid

phase turbulence. These effects were generally ignored in the earlier computational models for two-phase flows.

Note also that the effects of wake-mechanism generating gas-phase turbulence (Yuan & Michaelides, 1992; Abu-Zaid & Ahmadi, 1993), which is expected to be small, is not included in [6]. The expression for the phasic momentum interactions described by Ahmadi & Ma (1990) includes the lift force. However, in [1] and [3], the effect of the lift force is also neglected.

Eliminating dp^f/dy between [2] and [4], it follows that

$$F_1 \frac{dv}{dy} = F_2, \tag{17}$$

where F_1, F_2 and C are given as:

$$F_1 = Cvk^f + (1-v)vk\frac{d\gamma}{dv} + (1-v)\gamma k, \tag{18}$$

$$F_2 = Cv(1-v)\frac{dk^f}{dy} - (1-v)v\gamma\frac{dk}{dy}, \tag{19}$$

$$C = \frac{2}{3}\frac{\rho_0^f}{\rho_0}. \tag{20}$$

Two-equation model for two-phase turbulent flow

The two equation κ–ϵ model was widely used for simulating single fluid phase turbulent flows. In most earlier studies, the logarithmic law-of-wall was used as a boundary condition near a solid wall. To be able to continue the flow domain to the wall, two-equation models for low Reynolds number flows were developed by Launder & Spalding (1972), Jones & Launder (1972), Lam & Bremhorst (1981), Chien (1982), Nagano & Hishida (1987), Wilcox (1988) and Fan *et al.* (1993), among others. For two-turbulent flows, prescribing the appropriate boundary conditions has always been a serious problem. In particular, the law-of-wall is no longer applicable except for high dilute mixtures. Therefore, for handling non-dilute flows, a suitable near wall (low Reynolds number) turbulence model for fluid phase is needed.

In the present study, the two-equation k–ϵ model of Chien (1982) is extended for application to fluid phase turbulence analysis in two-phase flows. The turbulence viscosity is assumed to be given as:

$$\mu^{fT} = C^{\mu^f}\rho_0^f v^f f^{\mu^f}(k^f)^2/\tilde{\epsilon}^f, \tag{21}$$

where the dissipation variable $\tilde{\epsilon}^f$ satisfies the following transport equation:

$$\rho_0^f v^f\frac{\partial\tilde{\epsilon}^f}{\partial t} = f_1 C^{c1}\frac{\tilde{\epsilon}^f}{k^f}\mu^{fT}\left(\frac{\partial u^f}{\partial y}\right)^2 - f_2 C^{c2}\frac{\tilde{\epsilon}_{f2}}{k^f} + E + \frac{\partial}{\partial y}\left[(\mu^f + \mu^{fT}/\sigma^{cl})\frac{\partial\tilde{\epsilon}^f}{\partial y}\right]. \tag{22}$$

The dissipation ϵ^f is given as:

$$\epsilon^f = \tilde{\epsilon}^f + \epsilon_0^f, \tag{23}$$

where ϵ_0^f is the extra dissipation. In these equations, the damping functions f^{μ^f}, f_1, f_2, E and ϵ_0^f are given as:

$$f^{\mu^f} = 1 - e^{-0.0115y^+}, \tag{24}$$

$$f_1 = 1, \tag{25}$$

$$f_2 = 1 - 0.22e^{-(Re_T/6)^2}, \tag{26}$$

$$E = -\frac{2\mu^f}{\rho_0^f v^f}\frac{\tilde{\epsilon}^f}{y^2}e^{-y^+/2}, \tag{27}$$

$$\epsilon_0 = 2\frac{\mu^f}{\rho_0^f v_f}\frac{k^f}{y^2}, \tag{28}$$

where Re_T and y^+ are defined as

$$\mathrm{Re}_T = \frac{\rho_0^f v^f k^{f2}}{\tilde{\epsilon}^f \mu^f}, \quad y^+ = \frac{\rho_0^f v^f u^* y}{v^f}, \tag{29}$$

in which $u^* = \sqrt{\tau_w/\rho_0^f v^f}$ is the shear velocity, and τ_w is the gas shear stress at the wall.

The values of the coefficients C^{μ^f}, $C^{\epsilon 1}$, $C^{\epsilon 2}$ and $\sigma^{\epsilon f}$ are given as:

$$C^{\mu^f} = 0.09 C^{*\mu^f}, \quad C^{\epsilon 1} = 1.35, \quad C^{\epsilon 2} = 1.80, \quad \sigma^{\epsilon f} = 1.3. \tag{30}$$

In [30], the coefficient $C^{*\mu^f}$ is also introduced to account for the effect of higher particulate solid volume fraction on damping the fluid turbulence, and is given as:

$$C^{*\mu^f} = \frac{1}{1 + \dfrac{\tau}{T_L}\left(\dfrac{v}{v_m}\right)^3} \tag{31}$$

When particulate volume fraction approaches zero, the flow becomes that of a single fluid phase. The coefficient C^{μ^f} then approaches 0.09, which matches that used by Chien (1982).

Boundary conditions

Due to symmetry, the boundary conditions at the channel centerline are

$$\frac{\partial u}{\partial y} = 0, \quad \frac{\partial u^f}{\partial y} = 0, \tag{32}$$

$$\frac{\partial k}{\partial y} = 0, \quad \frac{\partial k^f}{\partial y} = 0, \tag{33}$$

$$\frac{\partial \tilde{\epsilon}^f}{\partial y} = 0. \tag{34}$$

In addition, the global conservation of mass implies that

$$m = \frac{\displaystyle\int_0^H \rho_0 v u \, \mathrm{d}y}{\displaystyle\int_0^H \rho_0^f v^f u^f \, \mathrm{d}y} = \text{const.} \tag{35}$$

where m is the ratio of particle-to-gas mass flow rates (loading) and H is the half-width of the channel. At the wall, no-slip boundary conditions for fluid phase are used. These are

$$u^f = 0, \quad k^f = 0, \quad \tilde{\epsilon}^f = 0. \tag{36}$$

Boundary conditions for the particulate phase at the wall are much more complicated than those for the fluid phase. The experimental and digital simulation results for granular flows indicate that occurrence of slip at the wall is a common feature, and thus, the no-slip boundary conditions are no longer valid. For relatively small values of the coefficient of sliding friction μ_w for granular materials, Jenkins (1992) showed that the tangential momentum balance and fluctuation kinetic energy balance required

$$S = -\mu_w N, \tag{37}$$

and

$$K = -\tfrac{3}{8} N \sqrt{2k} [\tfrac{7}{2}(1 + r_w)\mu_w^2 - (1 - r_w)], \tag{38}$$

where r_w is the coefficient of restitution for a particle colliding with the wall. Here, the shear stress S, the normal stress N and the fluctuation kinetic energy flux K are given as:

$$N = \frac{\rho_0 \nu k}{3} [2(1 + 4\nu\chi) + (1 - r^2)], \tag{39}$$

$$S = (\mu + \mu^T) \frac{\partial u}{\partial y}, \tag{40}$$

$$K = -\kappa\sqrt{k}\frac{\partial k}{\partial y}, \tag{41}$$

where

$$\kappa = 0.0711\rho_0 d(1+r^2)(\chi^{-1} + 4.8v + 12.1184v^2\chi). \tag{42}$$

Equations [37] and [38] were derived based on the assumption that the coefficient of friction is so small that the point of contact of a particle always slips during a collision.

NUMERICAL PROCEDURES

Equations [1], [3], [5]–[8], [17] and [22] form a set of eight equations for determining the eight unknowns u, u^f, k, k^f, v, v^f, ϵ and ϵ^f. Since the governing equations are parabolic in nature, they can be solved numerically by the time marching forward method. That is, an initial solution is assumed to start the calculation and an iterative procedure is used until the final steady solution is reached.

The governing equations are discretized using the forward differencing in time and central differencing in space defined as

$$\frac{\partial}{\partial t} = \frac{(\,)_i^{(n+1)} - (\,)_i^{(n)}}{\Delta t}, \tag{43}$$

$$\frac{\partial}{\partial y} = \frac{(\,)_{i+1}^{(n+1)} - (\,)_{i-1}^{(n+1)}}{2\Delta y}, \tag{44}$$

Short hand notations

$$(\,)_{i+1/2} = [(\,)_i + (\,)_{i+1}]/2, \tag{45}$$

$$(\,)_{i-1/2} = [(\,)_i + (\,)_{i-1}]/2. \tag{46}$$

are also used in the subsequent analysis.

Equations [1], [3], [5], [6] and [22] in finite difference form may be, respectively, restated as

Particulate phase momentum balance

$$\begin{aligned}
&\Delta t\left(\frac{D_0}{\rho_0 v}\right)_i^{(n)} u_i^{f(n+1)} + \frac{1}{\rho_0 v_i^{(n)}}\frac{\Delta t}{(\Delta y)^2}(\mu+\mu^T)_{i-1/2}^{(n)} u_{i-1}^{(n+1)} \\
&\quad - \left\{1 + \frac{1}{\rho_0 v_i^{(n)}}\frac{\Delta t}{(\Delta y)^2}[(\mu+\mu^T)_{i-1/2}^{(n)} + (\mu+\mu^T)_{i+1/2}^{(n)}] + \Delta t\left(\frac{D_0}{\rho_0 v}\right)_i^{(n)}\right\} u_i^{(n+1)} \\
&\quad + \frac{1}{\rho_0 v_i^{(n)}}\frac{\Delta t}{(\Delta y)^2}(\mu+\mu^T)_{i+1/2}^{(n)} u_{i+1}^{(n+1)} = -u_i^{(n)} - \left(\frac{1}{\rho_0}\frac{dp^f}{dx} - g\right)\Delta t,
\end{aligned} \tag{47}$$

Fluid phase momentum balance

$$\begin{aligned}
&\frac{1}{\rho_0^f v_i^{f(n)}}\frac{\Delta t}{(\Delta u)^2}(\mu^f + \mu^{fT})_{i-1/2}^{(n)} u_{i-1}^{f(n+1)} \\
&\quad - \left\{1 + \frac{1}{\rho_0^f v_i^{f(n)}}\frac{\Delta t}{(\Delta y)^2}[(\mu^f+\mu^{fT})_{i-1/2}^{(n)} + (\mu^f+\mu^{fT})_{i+1/2}^{(n)}] + \Delta t\left(\frac{D_0}{\rho_0^f v^f}\right)_i^{(n)}\right\} u_i^{f(n+1)} \\
&\quad + \frac{1}{\rho_0^f v_i^{f(n)}}\frac{\Delta t}{(\Delta y)^2}(\mu^f+\mu^{fT})_{i+1/2}^{(n)} u_{i+1}^{f(n+1)} + \Delta t\left(\frac{D_0}{\rho_0^f v^f}\right)_i^{(n)} u_i^{(n+1)} \\
&= -u_i^{f(n)} - \left(\frac{1}{\rho_0^f}\frac{dp^f}{dx} - g\right)\Delta t,
\end{aligned} \tag{48}$$

Particulate phase kinetic energy balance

$$c_i^{(n)}\Delta t\left(\frac{2D_0}{\rho_0 v}\right)_i^{(n)} k_i^{\mathrm{f}(n+1)} + \frac{1}{\rho_0 v_i^{(n)}}\frac{\Delta t}{(\Delta y)^2}\left(\frac{\mu^{\mathrm{T}}}{\sigma^k}\right)_{i-1/2}^{(n)} k_{i-1}^{(n+1)}$$
$$-\left\{1+\frac{1}{\rho_0 v_i^{(n)}}\frac{\Delta t}{(\Delta y)^2}\left[\left(\frac{\mu^{\mathrm{T}}}{\sigma^k}\right)_{i-1/2}^{(n)}+\left(\frac{\mu^{\mathrm{T}}}{\sigma^k}\right)_{i+1/2}^{(n)}\right]+\Delta t\left(\frac{2D_0}{\rho_0 v}\right)_i^{(n)}\right\}k_i^{(n+1)}$$
$$+\frac{1}{\rho_0 v_i^{(n)}}\frac{\Delta t}{(\Delta y)^2}\left(\frac{\mu^{\mathrm{T}}}{\sigma^k}\right)_{i+1/2}^{(n)} k_{i+1}^{(n+1)} = -k_i^{(n)} - \Delta t\left\{\frac{\mu^{\mathrm{T}}}{\rho_0 v}\left(\frac{\partial u}{\partial y}\right)^2 - \epsilon\right\}_i^{(n)}, \qquad [49]$$

Fluid phase kinetic energy balance

$$\frac{1}{\rho_0^{\mathrm{f}} v_i^{\mathrm{f}(n)}}\frac{\Delta t}{(\Delta y)^2}\left(\mu^{\mathrm{f}}+\frac{\mu^{\mathrm{fT}}}{\sigma^{\mathrm{fk}}}\right)_{i-1/2}^{(n)} k_{i-1}^{\mathrm{f}(n+1)} - \left\{1+\frac{1}{\rho_0^{\mathrm{f}} v_i^{\mathrm{f}(n)}}\frac{\Delta t}{(\Delta y)^2}\left[\left(\mu^{\mathrm{f}}+\frac{\mu^{\mathrm{fT}}}{\sigma^{\mathrm{fk}}}\right)_{i-1/2}^{(n)}\right.\right.$$
$$\left.\left.+\left(\mu^{\mathrm{f}}+\frac{\mu^{\mathrm{fT}}}{\sigma^{\mathrm{fk}}}\right)_{i+1/2}^{(n)}\right]+\Delta t\left(\frac{2D_0}{\rho_0^{\mathrm{f}} v^{\mathrm{f}}}\right)_i^{(n)}\right\}k_i^{\mathrm{f}(n+1)} + \frac{1}{\rho_0^{\mathrm{f}} v_i^{\mathrm{f}(n)}}\frac{\Delta t}{(\Delta y)^2}\left(\mu^{\mathrm{f}}+\frac{\mu^{\mathrm{fT}}}{\sigma^{\mathrm{fk}}}\right)_{i+1/2}^{(n)} k_{i+1}^{\mathrm{f}(n+1)}$$
$$+\Delta t\left(\frac{2D_0}{\rho_0^{\mathrm{f}} v^{\mathrm{f}}}\right)_i^{(n)} k_i^{\mathrm{f}(n+1)} = -k_i^{\mathrm{f}(n)} - \Delta t\left\{\frac{\mu^{\mathrm{fT}}}{\rho_0^{\mathrm{f}} v^{\mathrm{f}}}\left(\frac{\partial u^{\mathrm{f}}}{\partial y}\right)^2 - \epsilon^{\mathrm{f}}\right\}_i^{(n)}, \qquad [50]$$

Dissipation variable transport equation

$$\frac{1}{\rho_0^{\mathrm{f}} v_i^{\mathrm{f}(n)}}\frac{\Delta t}{(\Delta y)^2}\left(\mu^{\mathrm{f}}+\frac{\mu^{\mathrm{fT}}}{\sigma^{\epsilon\mathrm{f}}}\right)_{i-1/2}^{(n)} \tilde{\epsilon}_{i-1}^{\mathrm{f}(n+1)} - \left\{1+\frac{1}{\rho_0^{\mathrm{f}} v_i^{\mathrm{f}(n)}}\frac{\Delta t}{(\Delta y)^2}\left[\left(\mu^{\mathrm{f}}+\frac{\mu^{\mathrm{fT}}}{\sigma^{\epsilon\mathrm{f}}}\right)_{i-1/2}^{(n)}\right.\right.$$
$$\left.\left.+\left(\mu^{\mathrm{f}}+\frac{\mu^{\mathrm{fT}}}{\sigma^{\epsilon\mathrm{f}}}\right)_{i+1/2}^{(n)}\right]\right\}\tilde{\epsilon}_i^{\mathrm{f}(n+1)} + \frac{1}{\rho_0^{\mathrm{f}} v_i^{\mathrm{f}(n)}}\frac{\Delta t}{(\Delta y)^2}\left(\mu^{\mathrm{f}}+\frac{\mu^{\mathrm{fT}}}{\sigma^{\epsilon\mathrm{f}}}\right)_{i+1/2}^{(n)} \tilde{\epsilon}_{i+1}^{\mathrm{f}(n+1)}$$
$$= -\tilde{\epsilon}_i^{\mathrm{f}(n)} - \Delta t\left[\mathrm{f}_1 C^{\epsilon 1}\frac{\tilde{\epsilon}^{\mathrm{f}}}{k^{\mathrm{f}}}\mu^{\mathrm{fT}}\left(\frac{\partial u^{\mathrm{f}}}{\partial y}\right)^2 - f_2 C^{\epsilon 2}\frac{\tilde{\epsilon}^2}{k^{\mathrm{f}}} + E\right]_i^{(n)}. \qquad [51]$$

Note also that [17] is solved directly by using the Runge–Kutta method.

The steps followed for obtaining the steady state solution of [47]–[51] by using the time-forwarding method were:

(1) The initial values of $u^{(n)}$, $u^{\mathrm{f}(n+1)}$, $k^{(n)}$, $k^{\mathrm{f}(n)}$, $v^{(n)}$, $v^{\mathrm{f}(n)}$, $\epsilon^{(n)}$, $\epsilon^{\mathrm{f}(n)}$, $\mu^{(n)}$, $\mu^{\mathrm{f}(n)}$, $\mu^{\mathrm{T}(n)}$ (for $n=0$) and time step length Δt were specified.
(2) Solutions of the system of [47] and [48] for $u^{(n+1)}$ and $u^{\mathrm{f}(n+1)}$, the system of [49] and [50] for $k^{(n+1)}$ and $k^{\mathrm{f}(n+1)}$ and [51] for $\tilde{\epsilon}^{\mathrm{f}(n+1)}$ were obtained.
(3) A fourth-order Runge–Kutta's method was used to solve [17] for $v^{(n+1)}$.
(4) Equations [7], [8], [16], [21] and [23] were used to obtain $v^{\mathrm{f}(n+1)}$, $\mu^{\mathrm{T}(n+1)}$, $\epsilon^{(n+1)}$, $\mu^{(n+1)}$, $\mu^{\mathrm{f}(n+1)}$, $\mu^{\mathrm{fT}(n+1)}$ and $\epsilon^{\mathrm{f}(n+1)}$.
(5) Steps [2]–[4] were repeated until the final steady solution is reached.

In step (1), the initially laminar velocity profiles for particulate and fluid phases u and u^{f} given as

$$u = 2U_0\left[\frac{y}{H}-\frac{1}{2}\left(\frac{y}{H}\right)^2\right], \quad u^{\mathrm{f}} = 2U_0\left[\frac{y}{H}-\frac{1}{2}\left(\frac{y}{H}\right)^2\right], \qquad [52]$$

are used. Here U_0 is the mean velocity across the duct. The initial profiles of k and k^{f} are prescribed by using the method suggested by Schmidt & Patankar (1991a, b)

$$k = k_0\left(\frac{u}{U_0}\right)^2, \quad k^{\mathrm{f}} = k_0^{\mathrm{f}}\left(\frac{u^{\mathrm{f}}}{U_0}\right)^2, \qquad [53]$$

where k_0 and k_0^{f} are given as:

$$k_0 = 1.5(I^{\mathrm{T}}u_0)^2, \quad k_0^{\mathrm{f}} = 1.5(I^{\mathrm{T}}u_0^{\mathrm{f}})^2, \qquad [54]$$

in which I^T is the initial non-dimensional turbulence intensity. (Here $I^T = 0.05$ is used.) The initial value of $\tilde{\epsilon}^f$ is assumed to be given as:

$$\tilde{\epsilon}^f = 0.1k^f \frac{\partial u^f}{\partial y}, \quad [55]$$

and the initial values of ν^f, μ^T, ϵ, μ, μ^f and μ^{fT} and evaluated from [7], [8], [16] and [21].

For the iteration in step (3), the under-relaxation procedure for evaluating $v^{(n+1)}$ is used. That is,

$$v_{new}^{(n+1)} = v_{old}^{(n+1)} + \omega[v^{(n+1)} - v_{old}^{(n+1)}], \quad [56]$$

where $v^{(m+1)}$ is the value directly obtained from [17], and ω is the under-relaxation constant. Typically, $\omega = 0.3$ was used in the computations.

To better resolve the rapid variations occurring near the wall, a special non-uniform mesh distribution in the y direction was used which still allowed use of the central difference formulas for uniform mesh. This was accomplished by employing the procedure of using n_1 intervals of mesh size Δy starting from the wall, continued with n_2 intervals of mesh size $2\Delta y$ and then n_3 intervals of mesh size $4\Delta y$, and so on. At the interface of different mesh sizes, say at point m, the derivatives with respect to y are approximated by central finite-difference formulas using points $m-2$, m and $m+1$ and the corresponding mesh size. Typically, four such regions with a total number of 101 grid points, a Δy of 3.31×10^{-5} m and a Δt of 10^{-4} s were used in this study.

RESULTS AND DISCUSSIONS

In this section, model predictions for mean gas velocity, mean particle velocity, and phasic turbulence intensities ($(\overline{u'^2})^{1/2}/u_c$) for different loadings are presented and compared with the experimental results of Tsuji *et al.* (1984). Using a laser-Doppler velocimeter (LDV), Tsuji *et al.* reported measurements of the phasic flow properties in a fully developed, two-phase, air–particle turbulent flow in a 30.5 mm vertical pipe. In their experiments, polystyrene spheres with a density of $\rho_0 = 1020$ kg/m^3 and diameters in the range 0.2–1 mm were suspended in air.

A restitution coefficient of $r = 0.9$, for particle–particle collisions, and $r_w = 0.7$, for particle–wall collisions and a coefficient of dynamic friction $\mu_f = 0.2$ between a particle and the wall are used in the present study. These values are consistent with the observation of Govan *et al.* (1989), who studied the trajectories of glass spheres transported in a small pipe under conditions similar to those of Tsuji *et al.* (1984). In the computation, the pressure gradient in the gas and the particle concentration at the wall are input and are adjusted until the gas velocity at the centerline and the mass loading ratio are within one percent of the experimentally measured values.

Model predictions for a single-phase air flow in the duct are presented in figure 2, and are compared with the experimental data of Tsuji *et al.* (1984) for an upward flow in a vertical pipe flow. Figure 2(a) shows the velocity profile which is normalized with the aid of the gas velocity at the centerline. It is observed that the predicted mean velocity is in good agreement with the experimental data except near the wall, where the model prediction is somewhat lower than the experimental data. This difference may be due to the fact that the present result is for a two-dimensional vertical channel, while the experimental results were for a pipe flow. Figure 2(b) presents the corresponding gas turbulence intensity ($\sqrt{k^f}$) profile. The experimental data of Tsuji *et al.* (1984) for RMS-axial fluctuating velocity is also shown in this figure for comparison. The agreement is quite reasonable, in spite of the fact that model predictions are for a vertical channel while the data are for a pipe flow. These results show that the present model can predict the features of the single-phase air turbulent flow in a duct.

Figure 3 presents the model predictions for the phasic flow conditions of air and 0.2 mm polystyrene sphere mixtures. Here, the mass loading ratio is $m = 1$, the centerline gas velocity is 18.9 m/s, and the flow Reynolds number based on mean gas velocity is 3.0×10^4. At this low solid volume fraction, figure 3(a) indicates that the gas velocity profile resembles that of a turbulent flow with a sharp gradient near the wall. The mean particle velocity profile is quite flat across the duct, with a significant relative velocity at the wall. In most parts of the channel, the particle velocity is smaller than the air velocity, except near the wall, where it becomes larger. This is because the

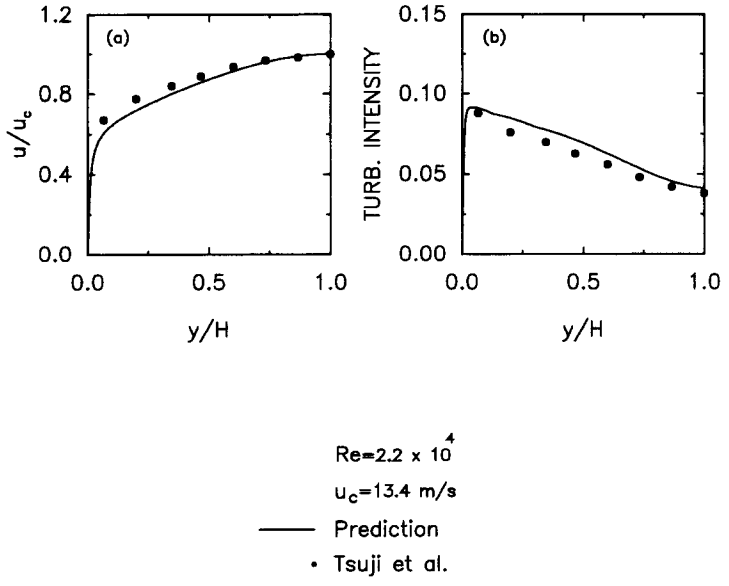

Figure 2. Variations of mean velocity and turbulence intensity profiles for clear gas. Comparison with the data of Tsuji *et al.* (1984).

air flow is subject to the no-slip condition at the wall, while the particle phase slips. Comparing figures 2(a) and 3(a), it is observed that the air velocity distribution becomes slightly more flat due to the presence of particles. The air and particle mean velocity profiles are compared with the experimental data of Tsuji *et al.* (1984) for a pipe in figure 3(a) While the predictions are in good agreement with the data, the model slightly over-predicts the gas velocity and under-predicts the particle velocity.

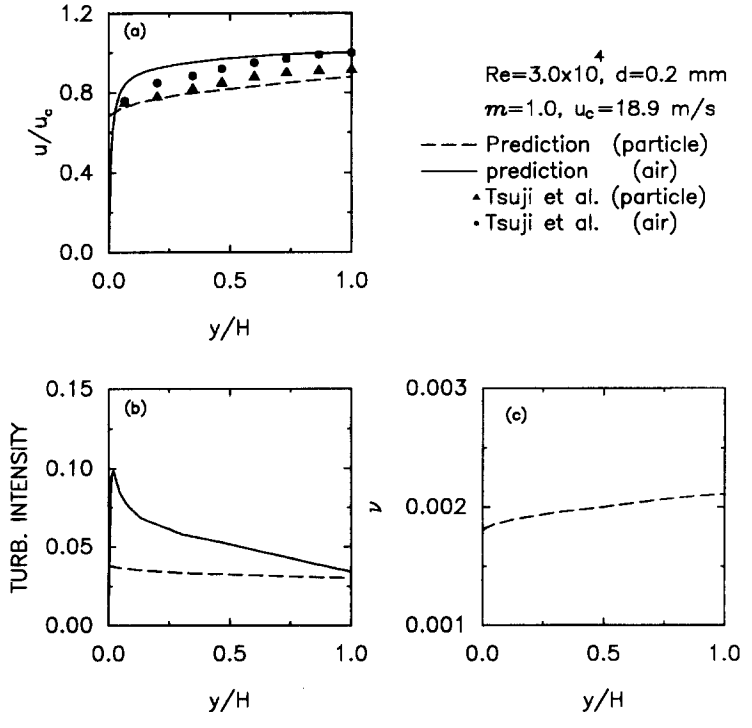

Figure 3. Variations of mean velocity, turbulence and solid volume fraction profiles for an air–0.2 mm particle mixture. Comparison with the data of Tsuji *et al.* (1984).

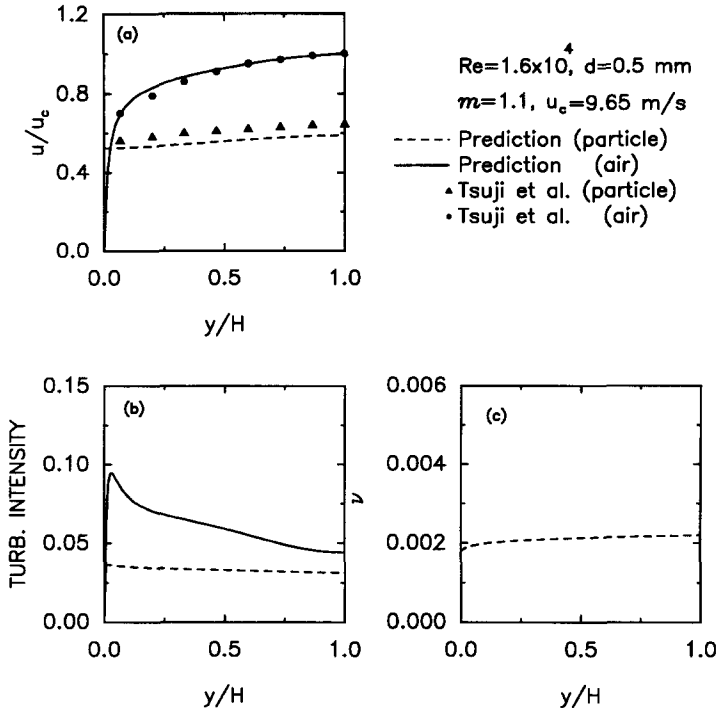

Figure 4. Variations of mean velocity, turbulence intensity and solid volume fraction profiles for an air–0.5 mm particle mixture. Comparison with the data of Tsuji *et al.* (1984).

Figure 3(b) shows the computed turbulence intensities of air and particulate phases. It is observed that the turbulence intensity of particulate phase is smaller than that of the air, and has a flat profile across the channel. The gas turbulence intensity profile has a shape similar to that of a clear gas. Comparing this profile with figure 2(b), it is noticed that the relative air turbulence intensity in the duct core is decreased. Thus, in this case, the presence of particles suppresses the air turbulence intensity. Figure 3(c) shows the solid volume fraction profiles across the channel. It is observed that the solid volume fraction is quite low (of the order of 0.002) and the particle concentration gradually increases toward the center of the channel. Unfortunately, the experimental data for turbulence intensity and concentration profiles were not reported for comparison.

Figure 4 compares the predicted phasic mean gas and particle velocities for an air–0.5 mm particle mixture with the experimental data of Tsuji *et al.* (1984). The corresponding phasic turbulence intensity and solid volume fraction profiles are also shown in this figure. In this case, the mass loading ratio is 1.1 and the air velocity at the channel centerline is 9.65 m/s. It is observed that the predicted mean air velocity is in good agreement with the experimental data, while the predicted particle velocity is slightly lower than the experimental results. Figure 4(b) indicates that the phasic air turbulence intensity is rather high near the wall, while the particulate phase turbulence intensity remains almost uniform. Figure 4(c) shows that the solid volume fraction is roughly constant across the channel.

For a mass loading ratio of 0.7 and a Reynolds number of 2.2×10^3, the model predictions are shown in figure 5. Here the particles are 0.5 mm polystyrene spheres and the flow is upwind. Figure 5(a) shows the mean air and particulate phasic velocities. The effect of the presence of particles on the air flow is similar to that of figure 3. The presence of particles somewhat flattens the mean air velocity distribution in comparison to the clear gas case. The velocity profile for the particulate phase is relatively flat and shows considerable slip at the wall. The particle mean velocity is also much lower than the gas velocity which is expected for these relatively large and heavy particles in an opposing gravitational field. The experimental data of Tsuji *et al.* (1984) are also reproduced in this figure for comparison. It is observed that the agreement between the measured and predicted

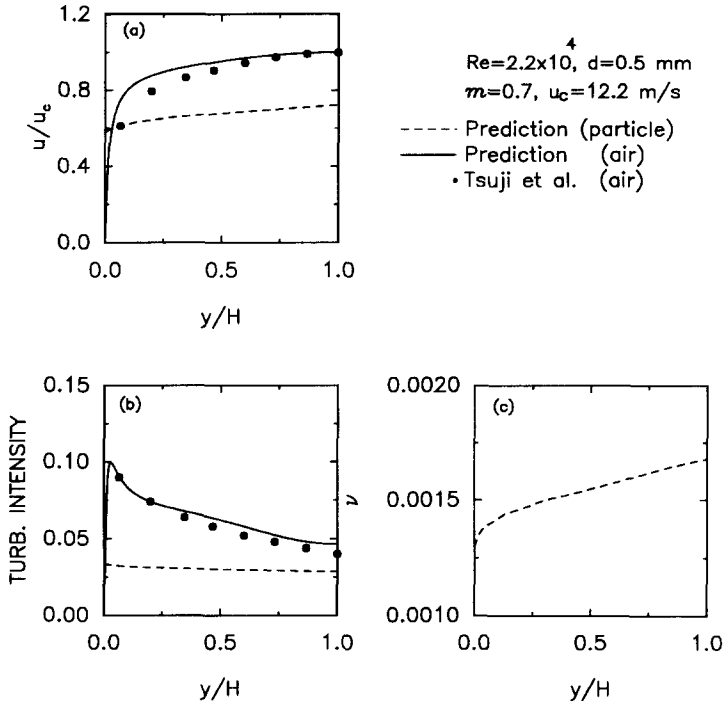

Figure 5. Variations of mean velocity, turbulence intensity and solid volume fraction profiles for an air–0.5 mm particle mixture. Comparison with the data of Tsuji *et al.* (1984).

mean fluid velocities is very good. Unfortunately, experimental data for the mean particulate velocity were not reported for a comparison to be made.

Turbulence intensities of gas and particulate phases are shown in figure 5(b). Similar to those in figure 3(b), it is observed that the air turbulence intensity is larger than that of the particulate phase. However, unlike the case of figure 3(b), the intensity of air turbulence is increased with the presence of particles. This figure also shows that there is an excellent agreement between the present model predictions and the experimental data for air turbulence intensity. Figure 5(c) presents the solid volume fraction profile. It is observed that v is of the order of 0.0015 and it is somewhat low near the wall and increases toward the channel centerline.

The model predictions for the variations of stresses in this case are shown in figure 6. Figure 6(a) shows the phasic normal stress profiles across the duct. It is observed that the normal stress for particulate phase is roughly constant, while the normal stress profile for gas phase has a sharp increase near the wall and then decreases toward the channel centerline. Figure 6(a) also shows that the normal stress for the gas phase is much larger than that of the particulate phase. Figure 6(b) shows the shear stress profiles for particulate and gas phases. It is observed that the shear stress for the gas phase has a relatively high value at the wall, and decreases to zero at the channel centerline. The shear stress of the particulate phase is very small at the wall, and increases to its maximum value at about 25% of channel half width. It then decreases to zero at the channel centerline. The total normal and shear stresses are presented in figure 6(c). It is noticed that the total normal stress has a very sharp peak near the wall region, and decreases gradually toward the channel centerline. The total shear stress has a nearly linear profile with its peak being at the wall.

Figure 7(a) presents the variations of the phasic momentum supply terms for particulate phase, $D_0(u^f - u)$, and gas phase, $D_0(u - u^f)$. This figure indicates that the momentum transfer for particulate phase is negative near the wall, and becomes positive at a very short distance from the wall and increases to about 175 N/m^{-3} at the channel centerline. This means that the particles receive momentum from the air in the entire channel except very near the wall where they transfer momentum to the air. As expected, the momentum supply term for the air is equal in magnitude and opposite in sign to that of particles. This is because the net phasic momentum transfer must be zero.

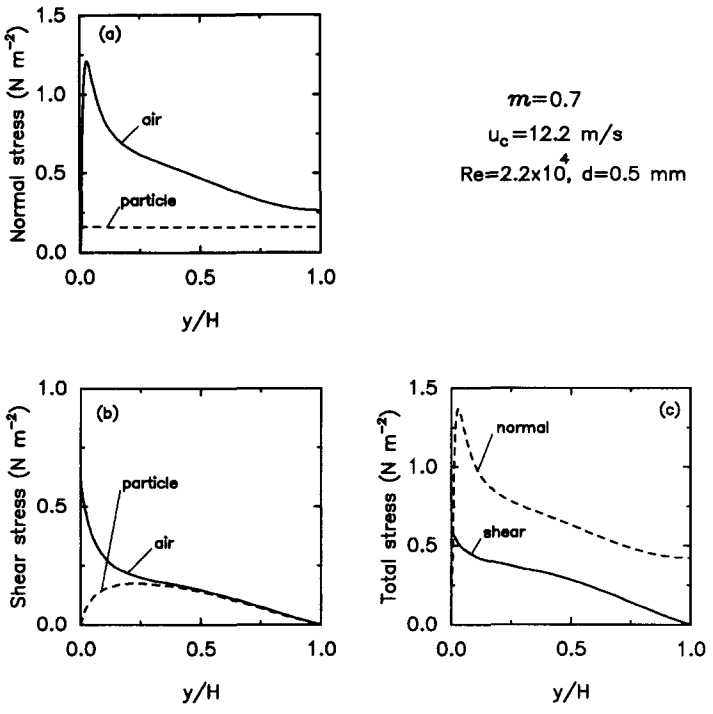

Figure 6. Variations of normal stress, shear stress and total stress profiles for an air–0.5 mm particle mixture.

The variation of the phase fluctuation energy supply for particulate phase $2D_0(ck^f - k)$ is shown in figure 7(b). It is observed that the energy supply for the particulate phase is negative, which implies that the fluctuation energy is transferred away from the particulate phase. The fluctuation energy supply profile is relatively flat across the channel except for a sharp decrease in magnitude near the wall.

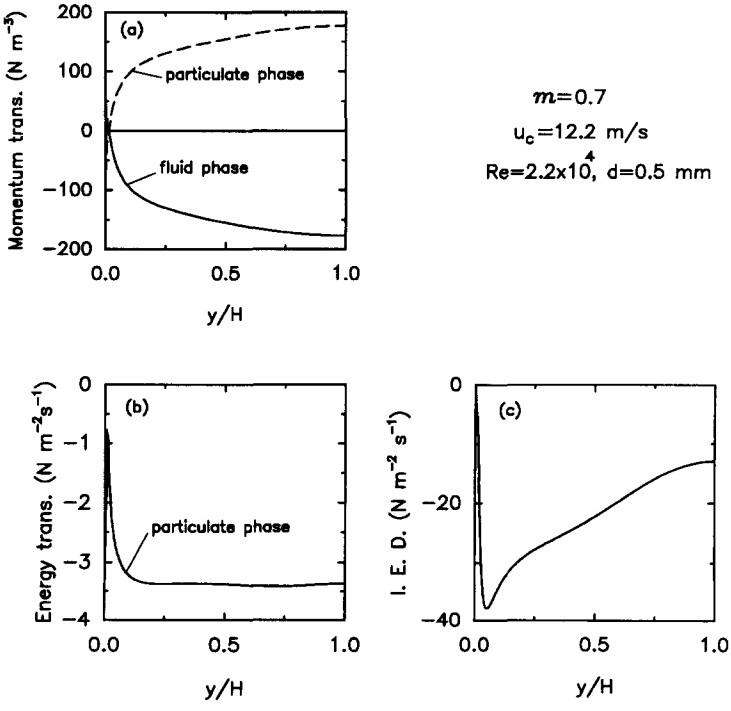

Figure 7. Variations of momentum and energy supply terms and interaction energy dissipation (IED) profiles for an air–0.5 mm particle mixture.

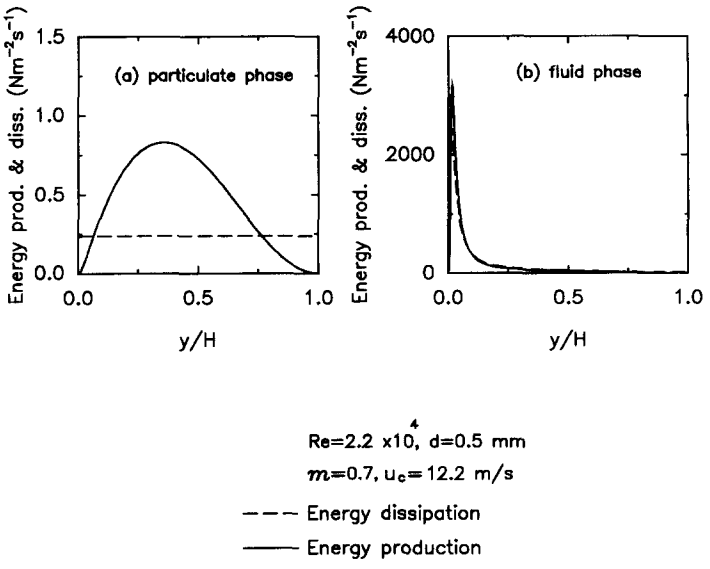

Figure 8. Variations of energy production and dissipation profiles for an air–0.5 mm particle mixture.

It should be emphasized that the fluctuation energy interaction process involves a significant amount of energy dissipation. Adding the interaction energy supply terms of [5] and [6] leads to the interaction energy dissipation given as:

$$\text{IED} = -2(1-c)D_0k^f, \qquad [57]$$

which is always negative indicating a loss of energy. Variation of the energy interaction dissipation profile is shown in figure 7(c). It is observed that the magnitude of the energy interaction dissipation reaches its maximum near the wall, and then decreases gradually toward the channel centerline.

The energy dissipation and production profiles for particulate and fluid phases are shown in figure 8. Figure 8(a) shows that the particulate energy dissipation is roughly constant across the flow region and is generally less than the energy production rate except in the neighborhood of the wall and the channel centerline. The particulate energy production is zero at the wall and at the centerline, and reaches its peak value at a distance of about one-third of the half-width of the channel from the wall. Figure 8(a) also shows that the net production of fluctuation energy exceeds the dissipation rate. Part of the excess energy is transferred to the fluid phase and the other part is consumed by the interaction energy dissipation. Figure 8(b) shows that the fluid phasic energy production and dissipation have sharp peaks near the wall, and decrease rapidly toward the channel centerline. These characteristics are typical of clear gas turbulence. From this figure, it is also observed that the energy production is somewhat larger than the dissipation rate. The excess fluctuation energy production balances the interaction fluctuation energy dissipation.

The phasic mean velocity, turbulence intensity and solid volume fraction profiles for air flow at a higher mass loading of $m = 3.4$ of 0.5 mm polystyrene spheres are shown in figure 9. In this case, the flow Reynolds number is $\text{Re} = 2.2 \times 10^3$ which is the same as that for figure 4. Figure 9(a) shows an interesting feature that the air mean velocity profile becomes concave and the location of maximum velocity deviates from the channel centerline. This phenomenon was observed in the experimental data of Tsuji *et al.* (1984), and was also reported by Vollheim (1965), who measured the mean air velocity in a vertical pipe in the presence of large particles at high loading ratios ($m = 1$–17) using a Pitot tube. Figure 9(a) indicates that the change of mass loading does not have a significant effect on the mean particulate velocity profile, and the wall relative velocity of particles of the same size and density. Figure 9(a) also shows good agreement between the model predictions and the experimental data of Tsuji *et al.* (1984).

Variations of turbulence intensities of particulate and gas phases are shown in figure 9(b). It is observed that the phasic turbulence intensities in the core region increase as the mass loading increases. The air turbulence intensity near the wall, however, is somewhat reduced as m increases.

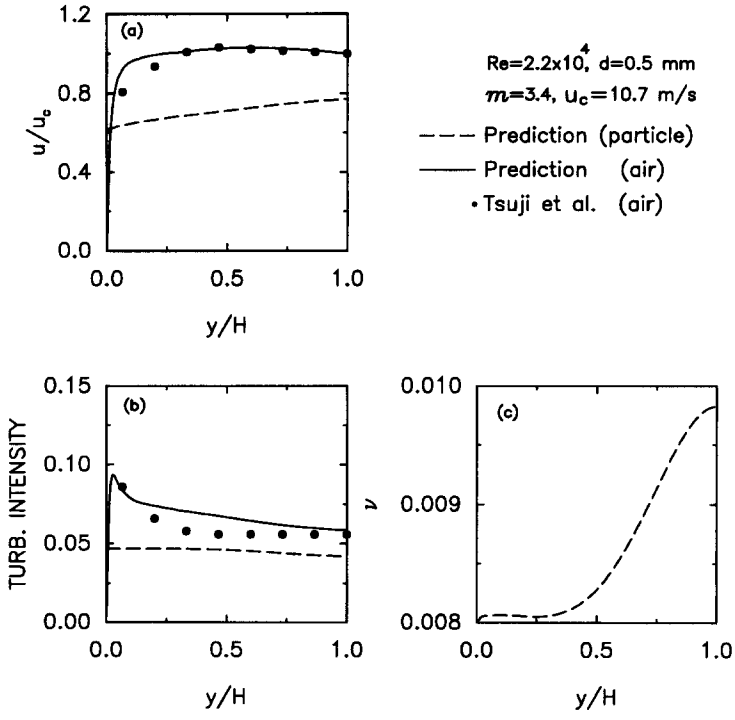

Figure 9. Variations of mean velocity, turbulence intensity and solid volume fraction profiles for an air–0.5 mm particle mixture. Comparison with the data of Tsuji *et al.* (1984).

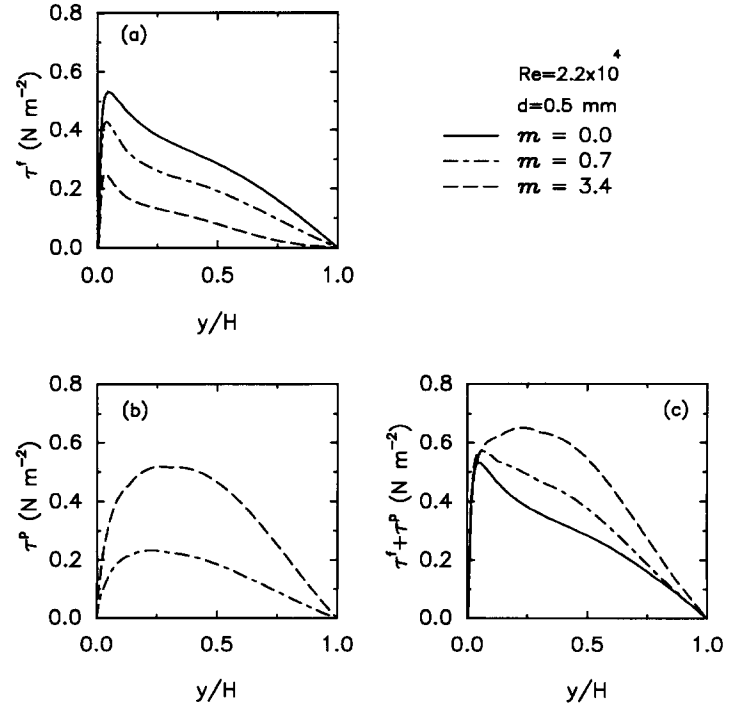

Figure 10. Variations of turbulence shear stress profiles for an air–0.5 mm particle mixture for different mass loading ratios.

The experimental data of Tsuji *et al.* (1984) for the turbulence intensity are reproduced in this figure and are in reasonable agreement with the present model predictions. Figure 9(c) presents the solid volume fraction profile across the duct. It is observed that the particle concentration increases toward the channel centerline. Comparing figure 9(c) with figure 4(c) shows that the variation of particle solid volume fraction is more rapid for a larger mass loading.

The influence of the mass loading ratio on the phasic turbulence shear stresses is shown in figure 10. Figure 10(a) indicates that the turbulence shear stress of the gas phase increases toward the wall reaching its maximum value at a distance of $y/H \approx 0.06$ to 0.08, and then decreases sharply to zero at the wall. As the mass loading ratio increases, the magnitude of the gas turbulence shear stress decreases. Figure 10(b) presents the particulate phase shear stress profiles at different mass loading ratios. It is observed that the shear stress of the particulate phase increases as m increases. This figure also shows that phasic particulate stresses are comparable to that of the gas phase even at these low solid volume fractions ($v = 0.002$ to 0.01). The total shear stress of the gas–particle mixture is shown in figure 10(c). This figure indicates that the total shear stress increases as mass loading ratio increases.

Figure 11 shows the model predictions for a two-phase gas–particle flow at a mass loading of $m = 0.6$ of 1 mm polystyrene spheres. The flow is upward and the Reynolds number in this case is 2.3×10^4. The maximum mean air velocity is $u_c = 13.4$ m/s which occurs at the channel centerline. Figure 11(a) shows the mean air and particle velocity profiles. The experimental data of Tsuji *et al.* (1984) for air velocity are also reproduced in this figure for comparison. It is observed that the model prediction for the air velocity is in good agreement with the experimental data. Compared with figure 4(a), it is found that the mean particle velocity is reduced and the relative slip between the particle and air velocity is increased significantly.

The phasic turbulence intensities are shown in figure 11(b). The air turbulence intensity has the general characteristic of clear air turbulence and the particle turbulence intensity profile is roughly constant across the duct. Compared with figure 2(b), it is observed that the air turbulence intensity generally increases due to the presence of 1 mm particles except very near the wall where it decreases. Thus, the particles promote turbulence in the core region while they suppress it near the wall. The experimental data of Tsuji *et al.* (1984) for air turbulence are reproduced in figure 11(b)

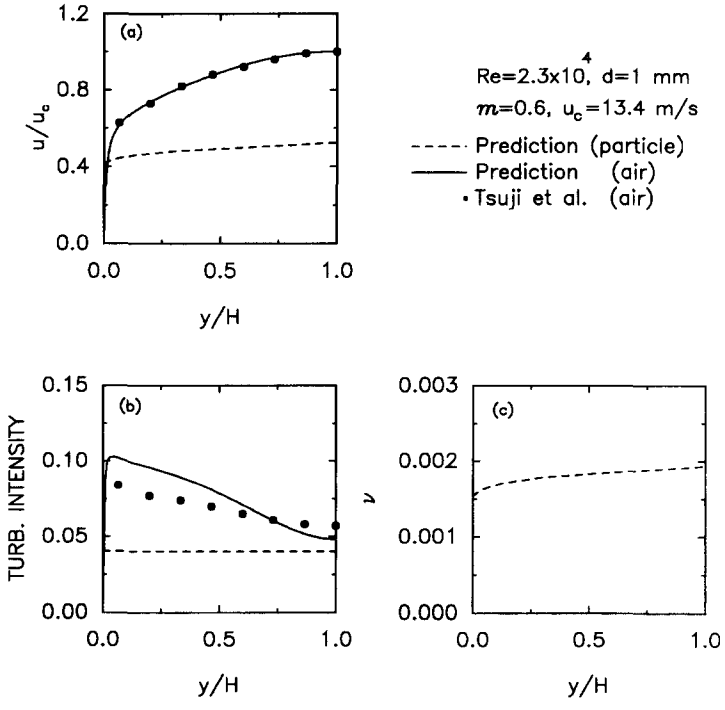

Figure 11. Variations of mean velocity, turbulence intensity and solid volume fraction profiles for an air–1 mm particle mixture. Comparison with the data of Tsuji *et al.* (1984).

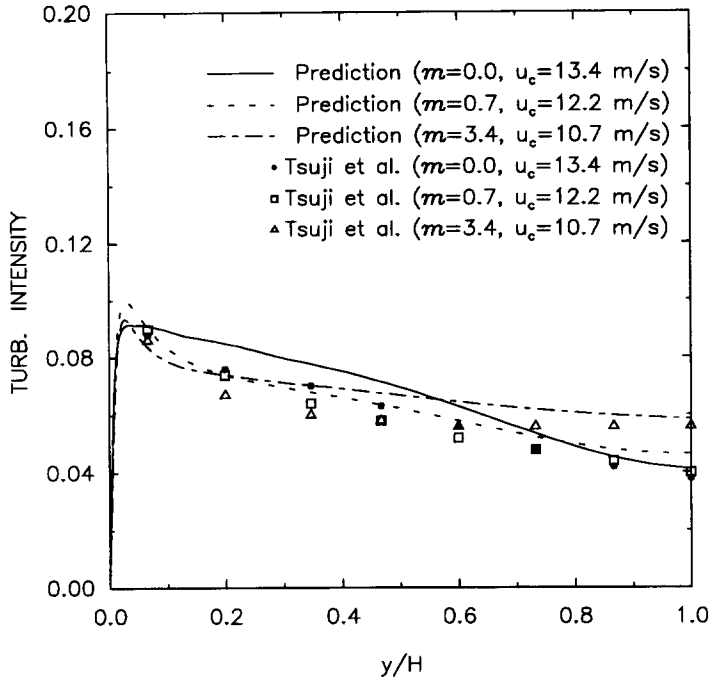

Figure 12. Variations of air turbulence intensity in the presence of 0.5 mm particles. Comparison with the data of Tsuji *et al.* (1984). $Re = 2.2 \times 10^4$.

and are in qualitative agreement with the model prediction. Figure 11(c) shows that the particle solid volume fraction profile is roughly constant at about 0.0018 and tends to increase toward the channel wall.

Variations of air turbulence intensity for different mass loadings of 0.5 mm particles are shown in figure 12. The experimental data of Tsuji *et al.* (1984) are also reproduced in this figure and show good agreement with the model predictions. It is observed that air turbulence intensity is generally high near the wall and decreases toward the channel centerline. When the particle mass loading ratio increases from 0 to 3.4, the air turbulence intensity decreases near the wall and increases near the channel centerline. This implies that the presence of particles redistributes the fluctuation kinetic energy, and the air turbulence intensity becomes more uniform.

Miller & Gidaspow (1992) performed an experimental study of gas–solid flows in a 7.5-cm clear acrylic vertical pipe. The pipe was 6.58 m in length and the particles were 150 μm FCC catalyst particles with a density of 1714 kg/m^3. They found that the particles move upward in the core region, while a downward motion near the wall was observed. Furthermore, the concentration near the wall becomes quite large. Their experimental data for mean particle velocity and solid volume fraction (measured at a height of 4.18 m) are reproduced in figure 13. The present model predictions for a vertical channel under the same conditions of particle size and particulate mean velocity are evaluated and the results are plotted in this figure for comparison. Here $r = 0.9$, $r_w = 0.75$ and $\mu_w = 0.2$ are used in numerical simulation. It is observed that the model prediction of mean particle velocity in figure 13(a) and solid volume fraction in figure 13(c) are in good agreement with the experimental data. In particular, the down-flow and high concentration of particles near the wall are well predicted by the model. The predicted average air velocity is 3.25 m/s, while the measured superficial gas velocity was 2.89 m/s. Since the experimental data are for a pipe flow, and the model predictions are for a two-dimensional channel, certain deviations should be expected. Figure 13(c) shows that the air fluctuation kinetic energy is larger than that of the particulate phase, and both air and particulate fluctuation kinetic energies are high near the wall and decrease toward the channel centerline.

For conditions of figure 13, the model prediction for the particle mass flux is shown in figure 14, and is compared with the experimental data of Miller & Gidaspow (1992). This figure shows

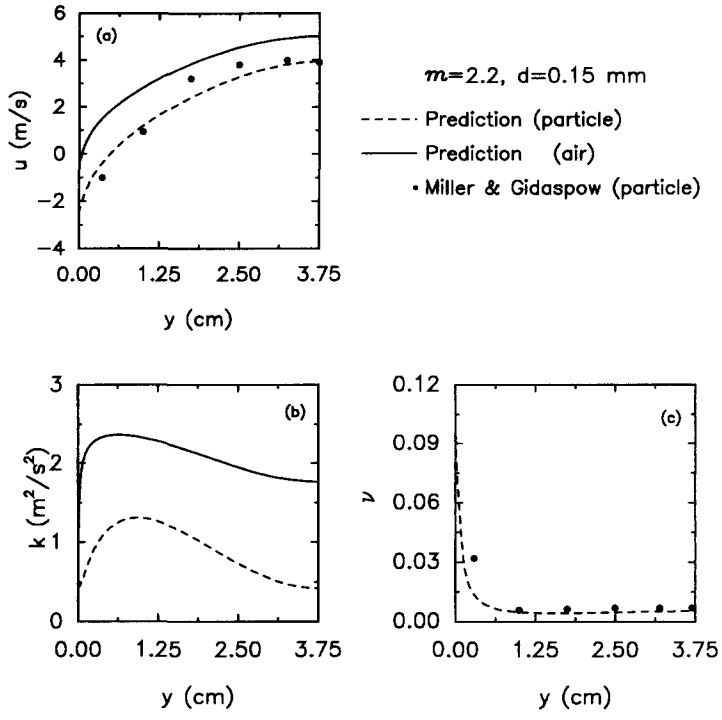

Figure 13. Variations of mean velocity, fluctuation kinetic energy and solid volume fraction profiles for an air–0.15 mm particle mixture. Comparison with the data of Miller & Gidaspow (1992).

that the particle mass flux is negative (downward) near the wall, increases rapidly and becomes positive (upward) at a short distance from the wall. The model prediction is also in reasonable agreement with the experimental data.

For a mass loading ratio of $m = 8.5$, figure 15 presents model predictions for a FCC catalyst particle–gas mixture and a comparison with the corresponding experimental data of Miller & Gidaspow (1992). The predicted average air velocity is 3.52 m/s, while the experiment was carried out at a superficial gas velocity of 2.61 m/s. Variations of the phasic mean velocity, fluctuation

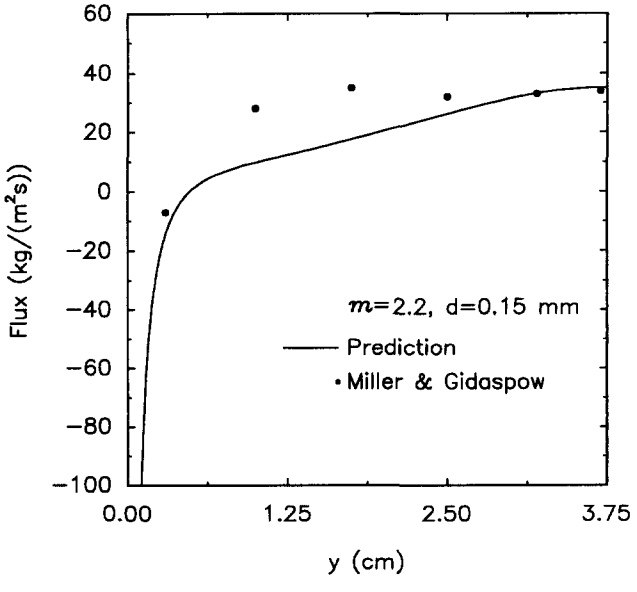

Figure 14. Variations of particle flux distribution for an air–0.15 mm particle mixture. Comparison with the data of Miller & Gidaspow (1992).

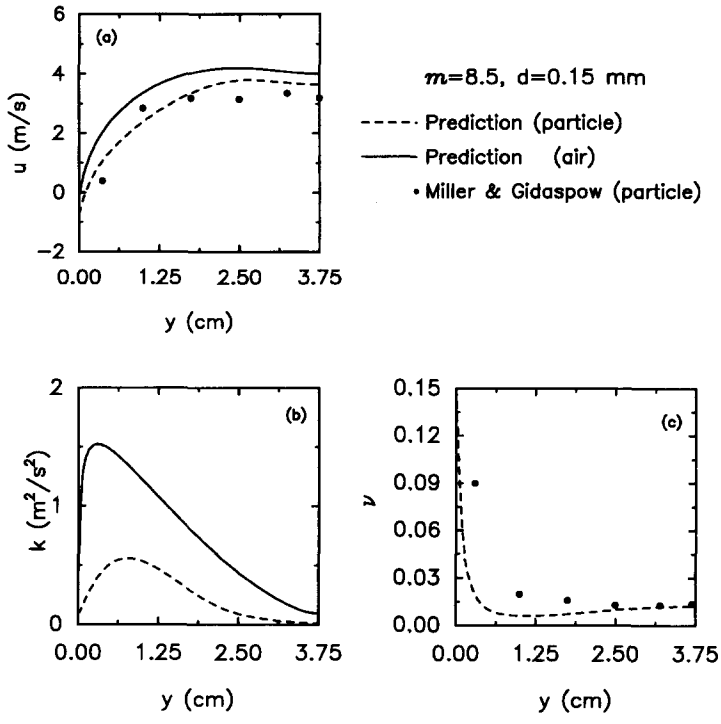

Figure 15. Variations of mean velocity, fluctuation kinetic energy and solid volume fraction profiles for an air–0.15 mm particle mixture. Comparison with the data of Miller & Gidaspow (1992).

kinetic energy and solid volume fraction are similar to those of figure 13. As the mass loading ratio increases, however, the particle down-flow velocity region becomes smaller. The phasic fluctuation kinetic energy decreases and decays more rapidly toward the channel centerline. Figure 15(c) shows that the particle concentration is higher and still maintains a sharp peak near the wall.

The sensitivity of particle mean velocity to the particle–wall friction coefficient μ_w is shown in figure 16. As μ_w increases from 0.1 to 0.3, the magnitude and range of particle down-flow velocity increase. This shows that the particle velocity near the wall is rather sensitive to the variation of

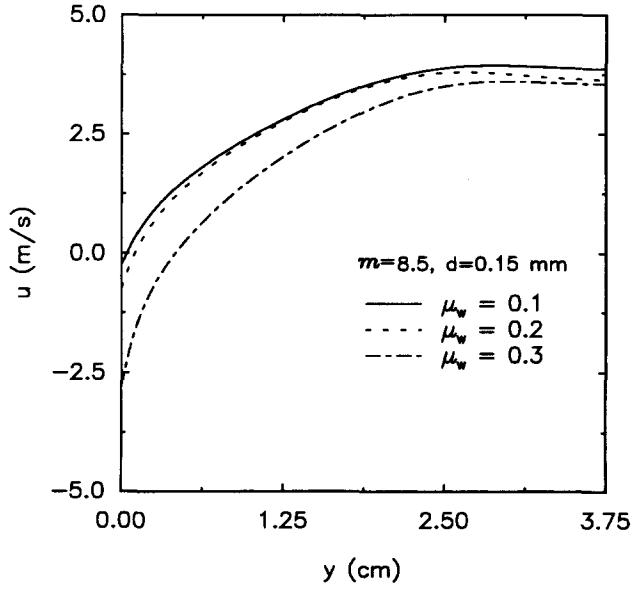

Figure 16. Variations of mean particle velocity for different particle–wall friction coefficients.

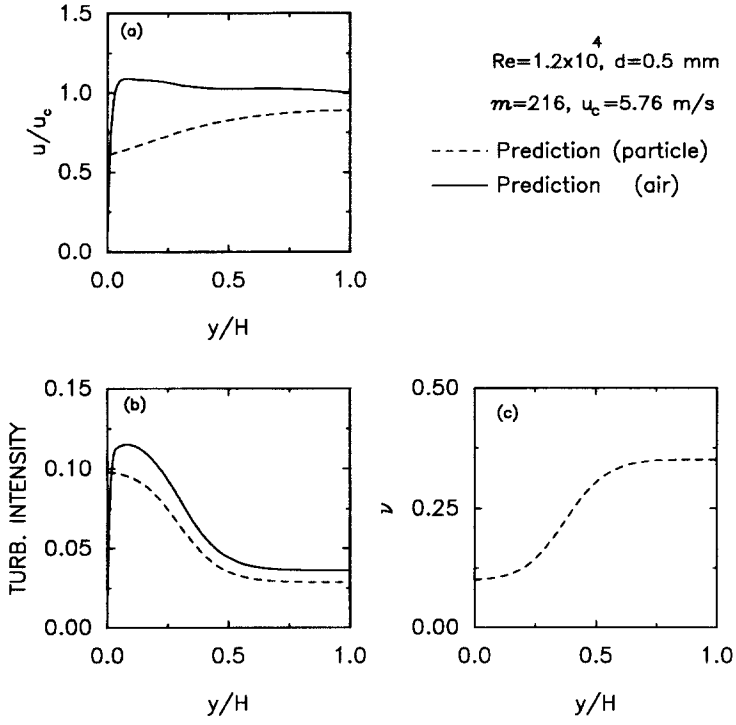

Figure 17. Variations of mean velocity, turbulence intensity and solid volume fraction profiles for an air–0.5 mm particle mixture.

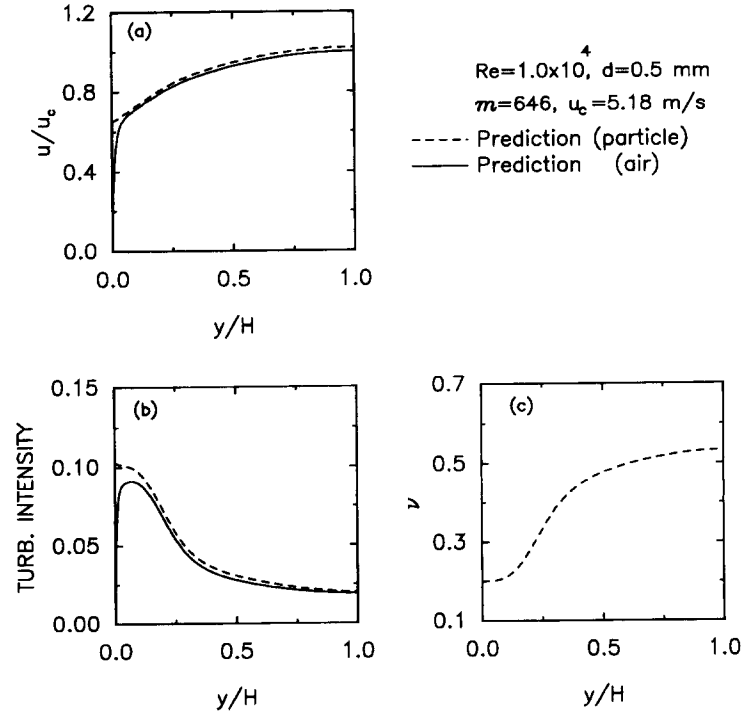

Figure 18. Variations of mean velocity, turbulence intensity and solid volume fraction profiles for an air–0.5 mm particle mixture. The flow is downward.

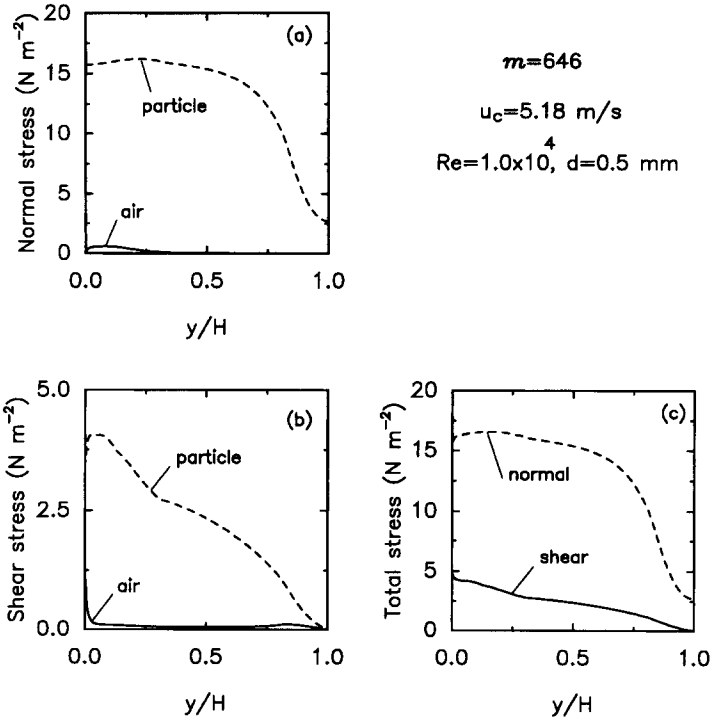

Figure 19. Variations of normal stress, shear stress and total stress profiles for an air–0.5 mm particle mixture. The flow is downward.

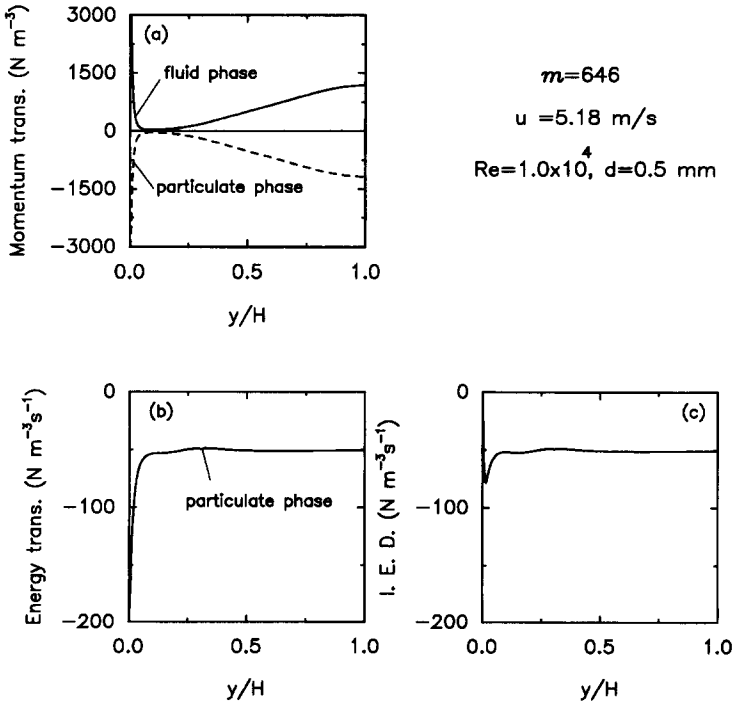

Figure 20. Variations of momentum and energy supply terms and interaction energy dissipation (IED) profiles for an air–0.5 mm particle mixture. The flow is downward.

μ_w. In particular, the frictional energy losses are important for proper prediction of the down-flow velocity region.

Figure 17 presents the model predictions for the phasic mean velocity, turbulence intensity, as well as the particulate solid volume fraction profiles for a relatively dense gas–particle mixture at a mass loading ratio of $m = 216$. The particles are assumed to be 0.5 mm polystyrene spheres and both air and particulate phase velocities are upward. Figure 17(a) shows the mean particulate and gas velocity profies. It is observed that the relative velocity between the air and particle decreases in the entire region when comparing with the dilute case. The concave shape of the air velocity profile also becomes more pronounced. The turbulence intensity profiles shown in figure 17(b) indicate that the particulate phase turbulence intensity increases comparing it with the dilute case and its profile becomes non-uniform. This is because the effect of particle–particle collision becomes more significant as the solid volume fraction increases. The gas turbulence intensity also increases and becomes quite uniform across the duct. Figure 17(c) shows the variation of the partciulate solid volume fraction profiles. It is observed that the solid volume fraction profile is strongly affected by the effects of inter-particle collisions and has a significant variation across the channel. Unlike the cases of figures 13 and 15, the volume fraction is realtively low near the wall and increases to a higher value in the centerline region.

Figures 18–21 present the model predictions for a gravity-driven flow of dense two-phase gas–particle mixture flow down a channel. In this case, the particles are 0.5 mm polystyrene spheres, the mass loading ratio is $m = 646$, the imposed pressure gradient is zero and the gas velocity at the channel centerlines is $u_c = 5.18$ m/s. Figure 18(a) shows the mean gas and particle velocity profiles. It is observed that the mean particulate velocity is generally slightly larger than that of the fluid phase. The relative velocity between the fluid and particulate phasic however, is quite large near the wall. This is because the flow is mainly driven by the particle weight. Figure 18(b) presents the turbulence intensity profiles for air and particulate phases. Unlike that of the dilute case, this figure shows that the particulate turbulence intensity is larger than that of the fluid phase, which is as expected for a collisional dominant particulate flow. Particle turbulence intensity also develops a spatial variation with a peak of about 0.11 near the wall and the fluid turbulence intensity has a maximum value of about 0.09 at $y/H = 0.1$. Both phasic turbulence intensities decay to 0.02 near the centerline.

The particulate solid volume fraction profile is shown in figure 18(c). It is observed that v is about 0.2 in the near wall region, then increases rapidly toward the channel centerline since both air and

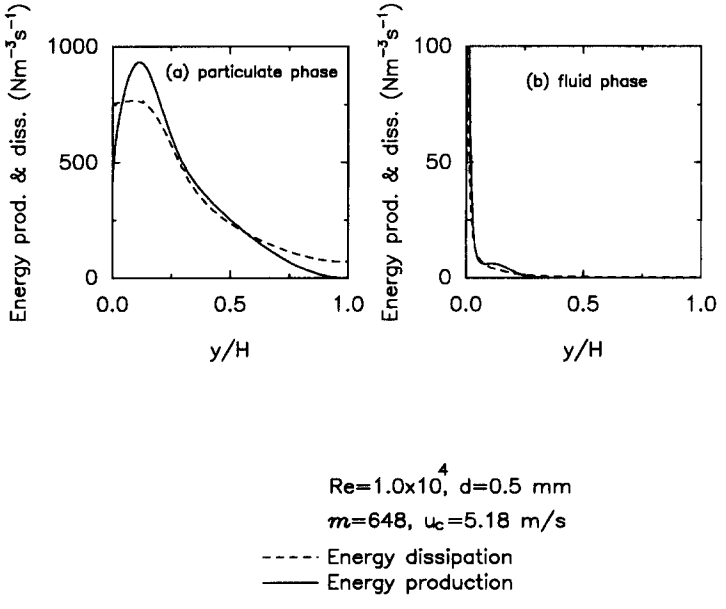

Figure 21. Variations of energy production and dissipation profiles for an air–0.5 mm particle mixture. The flow is downward.

particulate velocities are all downward. At the centerline the solid volume fraction reaches to its peak value of about 0.53.

The model predictions for the phasic stresses are shown in figure 19. Figure 19(a) and (b) shows the phasic normal and shear stress profiles for the air and the particles. It is observed that the particulate phasic stresses are much larger than those of gas phase for the gravity-driven dense flow. The fluid phasic stresses are generally negligible in comparison with those of the particulate phase. The particulate normal stress is roughly constant (about 16 N/m^2) for distances up to $y/H = 0.6$, and then decreases to a relatively small value of 2.5 N/m^2 at the channel centerline, while the corresponding shear stress has a decreasing trend. The total normal stress and shear stress profiles are shown in figure 19(c). This figure indicates that the total normal and shear stresses differ only slightly from those of the particulate phase. As expected, the total shear stress decreases almost linearly toward the channel centerline.

Figure 20(a) presents the model predictions for the phasic momentum supplies. As noted before, the phasic momentum supply terms are equal in magnitude and opposite in sign. This figure shows that the particles transfer momentum to the gas in the entire region. Figure 20(b) shows the variation of the interaction energy supply term, $2D_0(ck - k^f)$, for the particulate phase. It is observed that the energy supply term has a large magnitude, and is negative for the particulate phase implying that the fluctuation energy is transferred from the particulate phase to the fluid phase. The profile is also quite flat except near the wall where the interaction energy supply shows a sharp increase in magnitude. Figure 20(c) presents the model prediction for the interaction energy dissipation (IED), $-2D_0(1 - c)k^f$. It is observed that a significant loss of fluctuation energy occurs due to the interaction of particulate and gas phases.

Figure 21 shows the model predictions for the phasic fluctuation energy productions and dissipations. It is observed that the particulate fluctuation energy production and dissipation are much larger than their gas phase counterparts. The particulate fluctuation energy production also exceeds the particulate dissipation rate. The fluid phase production and dissipation rate show sharp peaks near the wall and decrease rapidly a short distance away from the wall. The excess particulate fluctuation energy production is, in part, transported to the gas phase and the rest is dissipated into heat through the phasic fluctuation energy interactions.

CONCLUSIONS

A thermodynamically consistent turbulence two-phase flow model is used to simulate dilute and dense flows of gas–solid mixtures in a vertical channel. The model predictions for the flow properties of particulate and gas phases are compared with the available experimental data and good agreement is observed. Based on the presented results, the following conclusions may be drawn:

(1) The fluctuation energies of gas and particulate phases strongly affect the behavior of two-phase turbulent flows.
(2) In addition to the interaction momentum supply, the interaction fluctuation energy supply is important and must be accounted for in the analysis of two-phase flows.
(3) For pressure gradient-driven two-phase gas–solid flows, the gas velocity is larger than the particle velocity. As a result the momentum is continuously supplied from the gas phase to the particulate phase. The effect of gravity is secondary and leads only to a small difference in the mean relative slip between particle and gas velocities.
(4) For a mass loading ratio of 0.6 or larger, the particulate fluctuation energy and its collisional production are important and affect the dynamic behavior of two-phase flows. In many cases, production of particulate fluctuation energy exceeds its dissipation rate. As a result, the presence of particles promotes turbulence in the gas phase. However, for some cases, the presence of very small particles may reduce the turbulence in the gas phases.
(5) The gas phase velocity profile becomes more flat due to the presence of particles. The larger the mass loading ratio, the flatter the mean air velocity profile becomes. The particle velocity profile is generally flat in most of the duct and exhibits a large slip at the wall.

(6) When the particulate phase moves upward in the same direction as the gas flow in the entire cross section, the solid volume fraction increases gradually toward the center of channel. When the particle flow near the wall is downward, the concentration becomes very large near the wall and decreases rapidly toward the channel centerline.
(7) For dilute flows, the normal and shear stresses of the particulate phase are smaller than those of the fluid phase. For dense flows, the normal and shear stresses of the particulate phase are much larger than those of the fluid phase, and control the behavior of the flow.
(8) For both dilute and dense flows, the energy production of particulate and fluid phases is larger than their energy dissipations in most parts of the flow region except near the wall and the channel centerline regions. There is a significant energy dissipation because of fluid–particle interactions.
(9) The model predictions for the vertical channel are in reasonable agreement with the experimental data of Tsuji *et al.* (1984) and Miller & Gidaspow (1992) for vertical pipes.
(10) The model reduces to the kinetic theory of granular material in the limit of dense collisional flows. Verification of mdoel predictions for nearly dense flows, however, must await the availability of appropriate experimental data.

Acknowledgements—The authors would like to thank Professor Tsuji for making the details of his data available to them. This work was supported by the U.S. Department of Energy (University Coal Research Program, PETC) under Grants DE-FG22-91PC91297 and DE-FG22-94PC213.

REFERENCES

Abu-Zaid, S. & Ahmadi, G. 1993 A thermodynamically consistent rate dependent model for turbulent two-phase flows—I. Formulation. Report No. MAE-281, Clarkson University, Potsdam, NY. Also *Int. J. Nonlinear Mech.* In press.

Ahmadi, G. 1982 A continuum theory for two-phase media. *Acta Mech.* **44,** 299–317.

Ahmadi, G. 1985 Thermodynamics of multitemperature fluids with applications to turbulence modeling. *Appl. math. Model.* **9,** 271–274.

Ahmadi, G. & Ma, D. 1990 A thermodynamic formulation for dispersed multiphase turbulent flows—I. Basic theory. *Int. J. Multiphase Flow* **16,** 323–340.

Bagnold, R. A. 1954 Experiments on a gravity-free dispersion of large solid spheres in Newtonian fluid under shear. *Proc. R. Soc. Lond.* **A225,** 49–63.

Bowen, R. M. 1967 Toward a thermodynamics and mechanics of mixtures. *Arch. Rat. Mech. Anal.* **24,** 370–403.

Chen, C. P. & Wood, P. E. 1985 Turbulence closure model for dilute gas–particle flows. *Can. J. Chem. Engng* **63,** 349–360.

Chien, K. Y. 1982 Predictions of channel and boundary-layer flows with a low-Reynolds-number turbulence model. *AIAA Jl* **20,** 33–38.

Dasgupta, S., Jackson, R. & Sundaresan, S. 1994 Turbulent gas–particle flow in vertical risers. *AIChE Jl* **40,** 215–228.

Elghobashi, S. E. & Alou-Arab, T. W. 1983 A two-equation turbulence model for two-phase flows. *Phys. Fluids* **26,** 931–938.

Eringen, A. C. & Ingram, J. D. 1965 A continuum theory of chemically reacting media—I. *Int. J. Engng Sci.* **3,** 197–212.

Fan S., Lakshminarayana, B. & Barnett, M. 1993 Low-Reynolds-number k–ϵ model for unsteady turbulent boundary-layer flows. *AIAA Jl* **31,** 1777–1784.

Genchev, Z. D. & Karpuzov, D. S. 1980 Effects of the motion of dust particles on turbulence transport equations. *J. Fluid Mech.* **101,** 823–842.

Gidaspow, D. 1986 Hydrodynamics of fluidization and heat transfer: supercomputer modeling. *Appl. Mech. Rev.* **39,** 1.

Gidaspow, D., Shih, Y. T., Bouillard, J. & Wason, D 1989 Hydrodynamics of a lamella electrosetter. *AIChE J* **35,** 714–724.

Gidaspow, D., Bezbaruah, R., Miller, A. & Jayaswal, U. 1991 Dense transport and fluidization of solids in a gas or liquid using kinetic theory. *Joint DOE/NSF Workshop on Flow of Particulates and Fluids*, Worcester, MA.

Govan, A. H., Hewitt, G. F. & Ngan, C. F. 1989 Particle motion in the turbulent pipe flow. *Int. J. Multiphase Flow* **15,** 471–481.

Hanes, D. M. & Inman, D. L. 1985 Observations of rapidly flowing granular–fluid materials. *J. Fluid Mech.* **150,** 357–380.

Hetstroni, G. 1982 *Handbook of Multiphase Systems.* Hemisphere, New York.

Hetsroni, G. & Sokolov, M. 1972 Distribution of mass, velocity and intensities in a two-phase turbulent jet. *J. Appl. Mech.* **93,** 315.

Jenkins, J. T. 1992 Boundary conditions for rapid granular flow: flat, frictional walls. *J. Appl. Mech.* **59,** 120–127.

Johnson, G., Massoudi, M. & Rajagopal, K. R. 1991a Flow of a fluid–solid mixture between flat plates. *Chem. Engng Sci.* **46,** 1713–1723.

Johnson, G., Massoudi, M. & Rajagopal, K. R. 1991b Flow of a fluid infused with solid particles through a pipe. *Int. J. Engng Sci.* **29,** 649–661.

Jones, W. P. & Launder, B. E. 1972 Prediction of laminarization with a two-equation model of turbulence. *Int. J. Heat Mass Transfer* **15,** 301.

Kashiwa, B. 1987 Statistical theory of turbulent incompressible flows. Ph.D. thesis, Los Alamos National Laboratory, Report No. LA-11088T.

Lai, Y. G. & So, R. M. C. 1990 On near-wall turbulent flow modeling. *J. Fluid Mech.* **221,** 641–673.

Lam, C. K. G. & Bremhorst, K. 1981 A modified form of the k–ϵ model for predicting wall turbulence. *Trans. Am. Soc. Mech. Engrs, J. Fluids Engrs* **103,** 456–459.

Launder, B. E. & Spalding, D. B. 1972 *Mathematical Models of Turbulence.* Academic Press, London.

Lee, S. L. & Durst, F. 1982 On the motion of particles in turbulent duct flows. *Int. J. Multiphase Flow* **8,** 125–146.

Lounge, M. Y., Mastorakos, E. & Jenkins, J. T. 1991 The role of particle collisions in pneumatic transport. *J. Fluid Mech.* **231,** 345–359.

Ma, D. & Ahmadi, G. 1986 An equation of state for dense rigid sphere gases. *J. Chem. Phys.* **84,** 3449–3450.

Ma, D. & Ahmadi, G. 1990 A thermodynamic formulation for dispersed multiphase turbulent flows—II. Simple shear flows for dense Mixtures. *Int. J. Multiphase Flow* **16,** 341–351.

Massoudi, M. 1986 Application of mixture theory to fluidized beds. Ph.D. thesis, University of Pittsburgh, Pittsburgh, PA.

Miller, A. & Gidaspow, D. 1992 Dense, vertical gas-solid flow in a pipe. *AIChE Jl* **38,** 1801–1815.

Modarress, D., Wuerer, J. & Elghobashi, S. 1982 An experimental study of a turbulent round two-phase jet. *AIAA/ASME Joint Thermophysics, Fluids, Plasma and Heat Transfer Conference*, St Louis, MO.

Modarress, D., Tan, H. & Elghobashi, S. 1983 Two-component LDA measurement in a two-phase turublent jet. *AIAA 21st Aerospace Science Meeting*, Reno, NV.

Mostafa Abdel-Hamed Taha Aly Rizk 1985 A two-equation model for free and bounded two-phase flows. Ph.D. thesis, University of California, Irvine, CA.

Nagano, Y. & Hishida 1987 Improved form of the k–ϵ model for wall turbulent shear flows. *Trans. Am. Soc. Mech. Engrs, J. Fluids Engrs* **109,** 156–160.

Nunziato, J. W. & Walsh, E. K. 1980 On ideal multiphase mixtures with chemical reaction and diffusion. *Arch. Rational Mech. Anal.* **73,** 285–311.

Popper, J., Abuaf, N. & Hetsroni, G. 1974 Velocity measurements in a two-phase turbulent jet. *Int. J. Multiphase Flow* **1,** 715.

Savage, S. B. & McKeown, S. 1983 Shear stresses developed during rapid shear of concentrated cylinders. *J. Fluid Mech.* **127,** 453–472.

Schmidt, R. C. & Patankar, S. V. 1991a Simulating boundary layer transition with low-Reynolds-number k–ϵ turbulence models. Part 1—An evaluation of prediction characteristics. *Trans. Am. Soc. Mech. Engrs, J. Turbomach.* **113,** 10–17.

Schmidt, R. C. & Patankar, S. V. 1991b Simulating boundary layer transition with low-Reynolds-number k–ϵ turbulence models. Part 2—an approach to improving the predictions. *Trans. Am. Soc. Mech. Engrs, J. Turbomach.* **113,** 18–26.

Sinclair, J. L. & Jackson, R. 1989 Gas–particle flow in a vertical pipe with particle–particle interactions. *AIChE Jl* **35,** 1473–1486.

Sommerfeld, M., Ando, A. & Wennerberg, D. 1992 Swirling particle-laden flows through a pipe expansion. *J. Fluid Engng Trans. ASME* **114,** 648–656.

Soo, S. L. 1967 *Fluid Dynamics of Multiphase Systems.* Blaisdell, Waltham, MA.

Theofanous, T. G. & Sullivan, J. 1982 Turbulence in two-phase dispersed flows. *J. Fluid Mech.* **116,** 343–362.

Tsuji, Y. & Morikawa, Y. 1982 LDV measurements of an air–solid two-phase flow in a horizontal pipe. *J. Fluid Mech.* **120,** 385–409.

Tsuji, Y., Morikawa, Y. & Shiomi, H. 1984 LDV measurements of an air–solid two-phase flow in a vertical pipe. *J. Fluid Mech.* **139,** 417–437.

Tsuji, Y., Shen, N. & Morikawa, Y. 1989a Numerical simulation of gas–solid flows. Part 1—particle-to-wall collision. *Technol. Rep. Osaka Univ. Jap.* **39,** 233–241.

Tsuji, Y., Shen, N. & Morikawa, Y. 1989b Numerical simulation of gas–solid flows. Part 1—particle-to-wall collision. *Technol. Rep. Osaka Univ. Jap.* **39,** 243–254.

Truesdell, C. & Toupin, R. A. 1960 The classical field theories. In *Handbuck der Physik* (Edited by Flugge, S.), Vol. III/I. Springer, Berlin.

Vollheim, R. 1963 Verhalten der Wandschubspannung des Fördermediums beim pneumatischen Transport and Schußfolgerungen für den Wärmeü bergang. *Maschinenbautech* **12,** 233.

Wallis, G. B. 1969 *One-dimensional Two-phase Flow.* McGraw–Hill, New York.

Wilcox, D. C. 1993 Comparison of two-equation turbulence models for boundary layers with pressure gradient. *AIAA Jl* **31,** 1414–1421.

Yuan & Michaelides 1992 Turbulence modulation in particulate flows—a theoretical approach. *Int. J. Multiphase Flow* **18,** 779–785.

Zisselmar, R. & Molerus, O. 1979 Investigation of solid–liquid pipe flow with regard to turbulence modification. *Chem. Engng J.* **18,** 233.